CONTAMINATION OF BROAD-BAND PHOTOMETRY BY NEBULAR EMISSION IN HIGH REDSHIFT GALAXIES: INVESTIGATIONS WITH KECK'S MOSFIRE NEAR-INFRARED SPECTROGRAPH

Matthew A Schenker¹, Richard S Ellis¹ Nick P Konidaris¹, Daniel P Stark^{2,3},

Draft version October 30, 2018

ABSTRACT

Earlier work has raised the potential importance of nebular emission in the derivation of the physical characteristics of high redshift Lyman break galaxies. Within certain redshift ranges, and especially at $z \simeq 6-7$, such lines may be strong enough to reduce estimates of the stellar masses and ages of galaxies compared those derived assuming broad-band photometry represents stellar light alone. To test this hypothesis at the highest redshifts where such lines can be probed with ground-based facilities, we examine the near-infrared spectra of a representative sample of $20 \ 3.0 < z < 3.8$ Lyman break galaxies using the newly-commissioned MOSFIRE near-infrared spectrograph at the Keck I telescope. We use this data to derive the rest-frame equivalent widths (EW) of [O III] emission and show that these are comparable to estimates derived using the SED fitting technique introduced for sources of known redshift by Stark et al (2013). Although our current sample is modest, its [O III] EW distribution is consistent with that inferred for H α based on SED fitting of Stark et al's larger sample of 3.8 < z < 5 galaxies. For a subset of survey galaxies, we use the combination of optical and nearinfrared spectroscopy to quantify kinematics of outflows in $z \simeq 3.5$ star-forming galaxies, and discuss the implications for reionization measurements. The trends we uncover underline the dangers of relying purely on broad-band photometry to estimate the physical properties of high redshift galaxies and emphasize the important role of diagnostic spectroscopy.

Subject headings: galaxies: evolution

1. INTRODUCTION

Detailed photometry of Lyman Break galaxies undertaken with the Hubble Space Telescope (HST) and the Spitzer Space Telescope has provided spectral energy distributions (SEDs) for large samples of Lyman break galaxies (LBGs) in the important redshift range 3 < z < 7. These data have been used to derive valuable estimates of the star formation rates (SFRs), stellar masses and ages (e.g., Stark et al. 2009; Labbé et al. 2010; González et al. 2011). The stellar mass density is a particularly important measure for the epoch just after reionization ended, as it provides a key indication of whether yet earlier star formation at z > 6 is capable of maintaining cosmic reionization (Robertson et al. 2013).

In an earlier paper (Stark et al. 2013), we used our large Keck spectroscopic redshift survey of 3 < z < 7 LBGs (Stark et al. 2010; Stark, Ellis, & Ouchi 2011) to investigate earlier claims (Schaerer & de Barros 2009, 2010; Ono et al. 2010; de Barros, Schaerer, & Stark 2012) that emission from rest-frame optical nebular emission lines (e.g. [O II], [O III], $H\alpha$) may contaminate the broad-band fluxes uses to derive the above physical quantities. Examining the SEDs of galaxies of known spectroscopic redshift (provides a sounder basis for such an investigation compared to 'forward modeling' techniques, based on adding nebular emission to stellar population synthesis models, which cannot provide an unambiguous result using broad-band data alone. We used this tech-

³ Hubble Fellow

nique, pioneered in Shim et al. (2011) to compare SEDs in a redshift range 3.8 < z < 5.0 where line contamination is likely, with those in an uncontaminated range 3.1 < z < 3.6, and show that $H\alpha$ emission typically contributes 30% of the flux at $3.6\mu m$. From this comparison we derived a rest-frame equivalent width distribution for $H\alpha$ which was used to show that nebular emission is likely to have a significant impact for galaxies at $z \simeq 6-7$ where both warm IRAC filters are contaminated by [O III] and $H\alpha$.

An additional motivation for the Stark et al. (2013) study was our interest in addressing a puzzle which arose from early measures of the specific star formation rate (sSFR) for z > 2. It had been claimed that this quantity does not evolve strongly between $z \simeq 2$ and 7 (e.g., Stark et al. 2009; González et al. 2010) in contrast to numerical simulations (e.g., Davé, Finlator & Oppenheimer 2012a) which predict that the sSFR should closely match the inflow rate of baryonic gas. In Stark et al. (2013), we used the equivalent width distribution of $H\alpha$ derived from the Keck sample to show that the sSFR is likely to evolve more rapidly at z > 4 than previously thought, supporting up to a five-fold increase between $z \simeq 2$ and 7 (see also de Barros, Schaerer, & Stark 2012; c.f. González et al. 2012).

In this paper, we take the subject to the next logical stage by verifying directly with near-infrared spectroscopy, the impact of nebular emission in the analysis of SEDs for high redshift LBGs. Prior to the launch of the James Webb Space Telescope (JWST) it is not possible to directly examine contamination by $H\alpha$ emission within the IRAC warm filters. However, in a manner similar to that employed by Stark et al. (2013), we can

¹ Department of Astrophysics, California Institute of Technology, MC 249-17, Pasadena, CA 91125; schenker@astro.caltech.edu

² Department of Astronomy and Steward Observatory, University of Arizona, Tucson AZ 85721

investigate contamination by [O III] 5007 Å in the photometric K_S band at $2.2\mu m$ by studying a representative sample of 3.0 < z < 3.8 spectroscopically-confirmed LBGs. Our goal is to determine the rest-frame equivalent width distribution of [O III] directly, and to compare this to the extent possible with that inferred for $H\alpha$ from the SED-based study of Stark et al. (2013). Such a spectroscopic program is made possible by the arrival at the Keck 1 telescope of the multi-slit near-infrared spectrograph MOSFIRE (McLean et al 2012) which offers the advantage of a significant multiplex gain. Using this new instrument, we target a representative sample of LBGs selected to lie within the 3.0 < z < 3.8 redshift range in the GOODS North field. We can thus take advantage of ACS photometry from the GOODS survey and improved near-infrared photometry from the CANDELS survey. This extensive photometry further means we can directly compare measured [O III] fluxes with those inferred using the SED-based approach.

Throughout this paper, we adopt a Λ -dominated, flat universe with $\Omega_{\Lambda}=0.7$, $\Omega_{M}=0.3$ and $H_{0}=70\,\mathrm{h}_{70}~\mathrm{km}\,\mathrm{s}^{-1}\,\mathrm{Mpc}^{-1}$. All magnitudes in this paper are quoted in the AB system (Oke & Gunn 1983). We will refer to the HST ACS and WFC3/IR filters F435W, F606W, F775W, F850LP, F105W, F125W, and F160W as B_{435} , V_{606} , i_{775} , z_{850} , Y_{105} , J_{125} , H_{160} , respectively.

2. TARGET SELECTION

2.1. Photometry

For our target selection and SED fitting, it was necessary to assemble a full multi-wavelength catalog across the GOODS-N field. For the HST ACS data, we use the publicly available v2.0 GOODS-N mosaics (Giavalisco et al. 2004). For the newly-obtained CANDELS WFC3/IR data (Grogin et al. 2011; Koekemoer et al. 2011), we combine the single epoch mosaics publicly available as of March 2013 weighting by exposure time, using the image combination routine SWARP (Bertin et al. 2002). Our CANDELS reductions comprise the first 7 epochs taken in GOODS-N, and so a number of objects do not yet have coverage in the Y_{105} filter. However, as we have J_{125} and H_{160} , imaging for all targets, this does not constitute a significant weakness for our SED analyses.

To compute accurate colors for each object, we measured the flux of each object using isophotal apertures determined by SExtractor in PSF-matched images. Colors were corrected to a total magnitudes by computing the offset from MAG AUTO for the i_{775} band in the GOODS v2.0 catalog. In cases where MAG AUTO was deemed to be unreliable by visual inspection of the images, we instead used the offset to a flux measured in a 1.0" diameter aperture to derive a total magnitude.

For the key photometry in the spectral region of interest, we use the K_S -band image derived from ultra-deep Canada France Hawaii Telescope imaging published by Wang et al. (2010). This image has total exposure time t=49.4 hr and a 5σ limiting magnitude of 24.5 in the GOODS-N field. As the FWHM of the image is 0.7-0.8", we do not attempt to PSF-match the other images to this coarser resolution. Rather, as our objects are largely compact, we perform photometry in 1.0" diameter apertures, and apply a correction of 0.7 mag for flux

falling outside the aperture, determined from analyses of isolated, unsaturated stellar sources in the K_S image. Finally, where available, we use deconfused Spitzer IRAC 3.6 and 4.5 μ m photometry.

2.2. Spectroscopic Sample

Our primary source of targets consisted of spectroscopically-confirmed galaxies from the Keck survey of 3 < z < 6 LBGs (Stark et al. 2010; Stark, Ellis, & Ouchi 2011) in the GOODS-N field. Briefly, this sample was compiled via optical follow-up of color-selected Lyman break galaxies (B, v, and i-drops) with the DEIMOS spectrograph on Keck II. The relevant observations took place between 2008 and 2010, and integration times for the sample considered here ranged from 5.0 to 7.0 hours. The interested reader can find the full details of the sample in Stark et al. $(2010)^4$.

From this compilation, we chose to undertake nearinfrared spectroscopy of LBGs, primarily B-drops, with confirmed redshifts 3.0 < z < 3.8 since both H β and [OIII] 4959 + 5007 lie within the MOSFIRE K-band transmission window. As the original B-drop sample only sparsely populates the above redshift range, in anticipation of the present needs, we increased the available sample via further DEIMOS observations in June 2012 using photometric redshifts to improve the redshift coverage. To achieve this, we first created a catalog of B_{435} dropout galaxies using the GOODS v2.0 catalogs and the selection criteria outlined in Stark et al. (2009). These SEDs were then evaluated with a photometric redshift code to assess their chances of lying at $z \leq 3.8$. This is a key step, as the B-drop sample possesses a mean redshift of $z \sim 4.0$, and only $\simeq 25\%$ of B-drops lie below z = 3.8 (see Fig. 1). Our priorities for inclusion of these targets on the mask were the probability of lying at z < 3.8 and the z_{850} magnitude for each target, with brighter targets favored.

This investment of spectroscopic observing time enables us to select targets that are known *a priori* to lie in the accessible redshift range, and maximizes our efficiency. Additionally, in the event of non-detections of nebular emission lines, prior knowledge of the redshift affords robust upper limits on the fluxes.

Since we are interested in the nebular emission line properties of this sample, it is important to note that all the targets for the various DEIMOS campaigns were selected only using ACS photometry, and thus should not be significantly biased towards objects with strong nebular emission.

2.3. Photometric Sample

As MOSFIRE can accommodate as many as 46 slits on a single mask, we sought to augment our spectroscopic sample above with further photometrically-selected LBGs. Our procedure for adding new targets was largely as described above, except the SEDs now incorporated CANDELS WFC3 data where appropriate, and deconfused Spitzer IRAC photometry.

Although one of the goals of this campaign was to verify the technique pioneered in Shim et al. (2011) and

⁴ A final catalog of this extensive spectroscopic survey is now being prepared for publication (Stark et al, in prep)

Stark et al. (2013) of using photometric excesses to determine line strengths, we specifically avoided prioritizing targets by their K-band magnitude. This allows us to construct an unbiased sample, and thus a better estimate of the true distribution of nebular line equivalent widths in the following analysis.

3. OBSERVATIONS

The targets defined above were observed using MOS-FIRE (McLean et al. 2012) on the Keck II telescope. We observed two masks on separate observing runs. The first mask was observed on the night of March 20-21, 2013 for a total of 4.25 hours integration time, of which $\simeq 1$ hour was affected by thin cloud. The average seeing for this mask was 0.75 arcseconds full-width at half maximum (FWHM). Our second mask was observed on the night of Apr 16-17, 2013. We obtained a total of 2.50 hours of useful integration time, with approximately 40 minutes of thin clouds, and an average seeing of 0.70 arcseconds FWHM.

We used an ABAB dither pattern with individual exposures of 180 seconds and a slit width of 0.7 arcseconds for all targets. On each mask, in addition to our science targets, we also included a star with $K_{AB} < 19.0$ to use for flux calibration. This ensures accurate accounting for slit loss due to seeing and pointing errors, as the star is observed in exactly the same manner as all targets.

The data was reduced using the publicly available MOSFIRE data reduction pipeline⁵. Briefly, the pipeline first creates a median, cosmic-ray subtracted flat field image for each mask. Wavelength solutions for each slit are fit interactively for the central pixel in each slit, then propagated outwards to the slit edges to derive a full wavelength grid for each slit. The sky background is estimated as a function of wavelength and time using a series of B-splines and subtracted from each frame. The AB frames are differenced, stacked, rectified and output for use along with inverse variance-weighted images used for error estimation. Flux calibration was performed using the standard star on each mask, and agrees with a calibration made using a separate A0V standard star taken during twilight to < 10%. For our analysis, we assume a 15% error on the flux calibration in all calculations.

In total we examined 28 targets and secured suitable near-infrared spectra for 20 LBGs in the required redshift range 3.0 < z < 3.8. Of these 13 have pre-existing optical spectra from DEIMOS and 7 represent new MOS-FIRE spectroscopic confirmations determined from our photometric sub-sample (Section 2.3). Table 1 and Fig. 1 summarize the salient properties of the final sample.

4. ANALYSIS

The primary goal of this work is to verify or otherwise the conclusions of Stark et al. (2013) which examined the equivalent width distribution for $H\alpha$ emission for LBGs of known spectroscopic redshift in the range 3.8 < z < 5.0. A significant conclusion from this study was the remarkably strong emission deduced by SED fitting. Using near-infrared spectroscopy with MOSFIRE we can not only directly measure the equivalent width distribution of [O III] emission but also test the robust-

ness of the SED-fitting approach by comparing spectroscopic line fluxes with those inferred from broad-band photometry.

4.1. Equivalent width distribution

Even a cursory inspection of our MOSFIRE spectra revealed the presence of many intense line emitters. Figure 2 shows the 2-D spectra for 4 targets showing strong emission where the continuum remains undetected. To assemble the equivalent width (EW) distribution, we considered all objects with a spectroscopic detection in either our DEIMOS or MOSFIRE campaigns (Table 1). Our sample of 20 objects spans $2.97 \le z \le 3.77$ with a median of z = 3.47. To determine the continuum level necessary to measure the EW, we corrected the K-band photometry for the observed fluxes of any emission lines seen in the MOSFIRE spectra. Where one of the [OIII] doublet lines was partially or fully obscured by a skyline, we assumed its flux adopting a fixed 5007/4959 line ratio of 3.0. For those spectroscopic targets for which no significant line fluxes were detected in our MOSFIRE data, we derived 1- σ upper limits for each nebular line EW. The photometry for one of our targets, N33_19374, is likely contaminated by a nearby object. In this case, we made no attempt to correct for the flux falling inside our apertures from other objects, but estimate the EW as a lower limit.

Equivalent widths and errors were measured using a Bayesian Monte Carlo technique. Because our equivalent widths depend on the measured line fluxes both directly and indirectly, through the subtraction of the emission component from the Ks-band photometry, accurate errors are non-trivial and can be asymmetric. To account for this, we run a Monte Carlo simulation with N = 10000 trials for each galaxy. This simulation takes the actual measured line fluxes and K_S photometry, perturbs each by the appropriate error, then calculates the appropriate continuum magnitude and EWs. At each step, we apply a prior that the fluxes must not be negative, to ensure a distribution that reflects reality.

Table 2 presents the spectroscopic line measures and the rest-frame EW distribution of [O III] 4959 + 5007 is presented in Fig. 3. It is immediately clear that most have very intense emission lines with a median [OIII] EW of 280 Å. There is a significant tail to much higher values; two galaxies have EWs > 1000 Å, where the K_S -band photometry is dominated by line emission. Importantly, we see no significant difference in the distribution for those galaxies selected on the basis of their DEIMOS spectroscopy and those photometrically selected entirely for this study.

4.2. Comparison with Stark et al. 2013

Although the foregoing suggests that intense line emission sufficient to significantly influence the broad-band photometry is quite a common property of $z \simeq 3\text{-}4$ LBGs, we now turn to whether the EW distribution within the present sample of 20 LBGs supports the conclusions of Stark et al. (2013) who derived the EW distribution of $H\alpha$ from a larger sample of 45 LBGs with 3.8 < z < 5.0 using SED fitting.

Firstly, it is important to determine whether the LBG samples in the two studies are broadly comparable. In

⁵ https://code.google.com/p/mosfire/

Fig. 4 we demonstrate that the UV luminosity distribution for the two samples are fairly similar, with a median absolute magnitude $M_{UV}=-21.0$ for the Stark et al. (2013) objects compared to $M_{UV}=-20.0$ for our present sample. Since the UV luminosity correlates closely with the star formation rate and prominence of Lyman α emission (Stark et al. 2010), this suggests that their nebular emission properties should not be too dissimilar.

Stark et al. (2013) found that the strength of H α emission at $z \simeq 4.5$ could be fit well by a log normal distribution with $\log_{10}({\rm EW}~/~{\rm \AA}) = 2.57$ and $\sigma = 0.25$. To facilitate a comparison with the present [O III] data, we adopt a value of 2.2 for the flux ratio of [OIII] to H α , taken from the empirical compilation of (Anders & Fritze-v. Alvensleben 2003). This ratio is appropriate for a metallicity $Z = 0.2Z_{\odot}$, consistent with that inferred from a stack of LBG spectra at $z \sim 4$ (Jones, Stark, & Ellis 2012), as well as measurements of ionized gas in LBGs at $z \sim 3.5$ (Maiolino et al. 2008).

To simulate the expected [O III] EW distribution, we must also account for noise in both the K_S -band photometry and the line fluxes, which we incorporate using a Monte Carlo distribution using the uncertainties quoted earlier. The result is the curve in Fig. 3 which provides an acceptable fit to the MOSFIRE data and a secure confirmation of large nebular line equivalent widths. We also determine the best fit lognormal distribution to our measurements of [OIII] EW. For our total sample of 20 galaxies with either MOSFIRE-confirmed nebular emission lines, DEIMOS Ly α redshifts, or both, we find best-fit parameters of $\log_{10}({\rm EW}\ /\ {\rm A}) = 2.4$ and $\sigma = 0.35$. As this sample has a median redshift $\Delta z \sim 1$ below the Stark et al. (2013) sample, the slightly weaker than predicted line strengths are not surprising.

Since we also observe the H β line in several of our MOSFIRE spectra, this provides an alternative check on the expected strength H α at these redshifts. To compute the expected H α flux, we adopt Case B recombination and compute the differential reddening determined from the best fit SED assuming a Calzetti law (Calzetti et al. 2000). The stellar continuum at the location of H α is likewise estimated from the best fit SED. Taking the average derived H α EW for all 13 DEIMOS galaxies in our sample, we find a value of EW(H α) = 380 Å, providing further support for the strong lines derived in Stark et al. (2013).

4.3. Verifying the SED fitting method

In addition to verifying that our MOSFIRE data on [O III] emission is broadly consistent with the inferences for ${\rm H}\alpha$ deduced from SED fitting, we can perform one final check by applying the SED fitting method used by Stark et al. (2013) to the present sample and compare the inferred [O III] fluxes with those measured directly in the near-infrared spectra.

For all objects with either an IRAC 3.6 or 4.5 μ m detection, we predict the [O III] line flux using the SED fitting technique adopted by Stark et al. (2013). We fit a grid of Bruzual and Charlot 2003 (BC03) stellar continuum models to the observed photometry of each galaxy, excluding the K-band. For the best fitting SED, we then compute a synthetic K-band flux, and determine the emission line strength from the residual. This can

only be applied for 8 galaxies from Table 1 for which a detection is available in at least one IRAC filter.

We list the ratios of the SED-predicted flux to that actually observed for the 8 objects in Table 2. Overall, the results are in excellent agreement: only one object, N42_11065 is a catastrophic outlier, with a significant [O III] flux implied from the SED method, but with none observed with MOSFIRE.. The remaining 7 objects all have predicted to observed fluxes within a factor of 2.5, and 6 are within a factor ≤ 1.6 . Such an agreement provides a clear validation that the technique we used in Stark et al. (2013) can provide line strength measurements suitable for statistical purposes.

4.4. Ly α velocity offsets

Since we now possess sample of $z \simeq 3.5$ galaxies with both optical and near-infrared spectra, we can comment briefly on the prevalence of outflows. As is well known, a velocity offset is often observed between Ly α , which is easily resonantly scattered by hydrogen on its way out of a galaxy, and other nebular lines which trace directly the sites of star formation and provide a systemic redshift, (e.g., Shapley et al. 2003). In particular, Ly α is often observed with a positive velocity offset, suggesting those photons are only able to escape after being scattered by an outflowing HI wind on the far side of the galaxy and shifting out of resonance with any HI on the near side (Steidel et al. 2010).

Measures of this offset velocity at high-redshift can shed light on some outstanding issues related to cosmic reionization. Firstly, one of the major currently unknown variables that enters into reionization calculations remains f_{esc} , the escape fraction of ionizing photons from galaxies. Although recent measurements have found $f_{esc} \simeq 10\%$ at $z \sim 3$ (Nestor et al. 2013), direct measurements are impossible at higher redshifts, owing to the increased opacity of the intergalactic medium (IGM). A higher value ($\simeq 20\%$) is required to reproduce measurements of the IGM neutral fraction at high redshifts (e.g., Robertson et al. 2013; Kuhlen & Faucher-Giguère 2012). As any outflowing neutral gas will serve to extinguish ionizing radiation, an observed decrease in the velocity offset of Ly α , potentially indicating a lower covering fraction of neutral gas, would provide further support for an increased f_{esc} . The velocity offset is also of direct interest, as numerous experiments seeking to directly probe the ionization state of the IGM at z > 6 utilize the visibility of Ly α emission (e.g., Pentericci et al. 2011; Schenker et al. 2012; Ono et al. 2012). If Ly α escapes galaxies with a smaller velocity offset than previously believed, it is closer to resonance and more easily quenched by a neutral IGM.

To this end, we present the difference in the observed velocities of $\text{Ly}\alpha$ and the $\text{H}\beta+[\text{OIII}]$ for all objects with at least a 3σ line detection in Table 2 and Fig. 6. The left panel displays both stacked $\text{H}\beta+[\text{OIII}]$ (black) and $\text{Ly}\alpha$ (red) profiles, demonstrating the high-fidelity velocity measurements we are able to make with MOSFIRE. In the right panel, we present a compilation of $\text{Ly}\alpha$ velocity offset measurements, plotted as a function of redshift and $\text{Ly}\alpha$ EW.

As all of the 9 targets in our MOSFIRE sample show significant Ly α in emission (EW > 20Å), we must be careful not to draw conclusions by blindly comparing

this to the Steidel et al. (2010) sample at lower redshift, for which all objects have only modest equivalent widths. A more illuminating conclusion can perhaps be drawn by compiling the velocity offsets for other galaxies with strong Ly α emission, drawn here from McLinden et al. (2011); Finkelstein et al. (2011); Hashimoto et al. (2013). All have quite low offsets, with $\langle v_{Ly\alpha} \rangle = +149 \text{ km s}^{-1}$ for the entire sample of 17 objects, and $\langle v_{Ly\alpha} \rangle = +157 \text{ km s}^{-1}$ for our own 9. As the fraction of starforming galaxies displaying strong Ly α emission increases with redshift out to at least $z \sim 6$ (Stark et al. 2010), this data implies it may become easier for ionizing photons to escape if this correlation of large EW_{Ly\alpha} with $v_{Ly\alpha}$ trend is in fact caused by lower HI covering fractions.

5. DISCUSSION

We have shown, through near-infrared spectroscopy with MOSFIRE, that the main conclusions of our earlier work (Stark et al. 2013) are confirmed. A significant fraction of our 20 LBG targets show intense [O III] line emission and the EW distribution is broadly comparable with that inferred for H α from SED fitting for a larger sample. Moreover, where we can make a direct comparison within our own sample, the SED fitting method predicts [O III] line fluxes that are in reasonable agreement, given the uncertainties, with those measured directly with MOSFIRE.

One might worry that because our DEIMOS-confirmed objects mostly display large $\text{Ly}\alpha$ equivalent widths (a result of following up only secure confirmations with MOS-FIRE) that we are biasing our sample toward especially strong emitters. However, our additional photometric sample of 7 objects dissuades this notion. Although the samples remain modest in size, not only does the EW distribution appear similar (Fig. 3), but our largest equivalent width object, N33_18453, is also part of this photometric sample.

We can also examine, for our present sample, how our measured line emission affects the derived physical properties. Fig. 5 presents SEDs for a selection of our sample where the excess flux in the K_S band is clearly visible. We can fit the SEDs using both the entire photometric dataset, including the line-contaminated Ks filter, as well as that excluding the contaminated band. In both cases, we assume a stellar continuum only. In this trial, the median properties of the sample hardly change; there is no significant change in age, and the stellar mass is reduced by only 3% when correcting for line emission. This is be-

cause the IRAC 3.6 and 4.5 μm photometry provides a crucial measurement free from line contamination longward of the Balmer break. Thus the majority of existing measurements of SED-derived properties of LBGs at $z\sim 3$ which incorporate IRAC data, should not be significantly affected by [O III] emission, even though it is particularly intense.

A more illuminating test applies when the IRAC photometry is ignored, in which case the K_S filter becomes the only photometric measurement beyond the Balmer break. This is a more appropriate test of how SEDs are fit at z \sim 6-7, where both the 3.6 and 4.5 μ m IRAC filters are contaminated by [OIII] and H α , respectively. In this comparison, the implications of line emission are much more striking. The median mass for the line corrected SEDs is only 64% that of the mass determined using the contaminated photometry, and the median age is lowered by 30%. For the most intense emitters, N33_24311 and N33_18453, the masses can be reduced by factors of \simeq 20.

We have demonstrated here, for the first time with both robust spectroscopy and significant sample sizes, the strength of nebular emission in $z \geq 3$ LBGs, as well as significantly increased the number of the same galaxies with measurements of Ly α velocity offsets. The implications of such observations are extremely important for the high redshift universe. SED fitting at high redshifts must account for contamination of broadband filters by these strong lines to determine accurate stellar masses. These lines provide mounting evidence for a continued increase of the sSFR beyond z=2, which has only recently been suggested. The measurements of precise offsets also provide valuable input to models which seek to map out the universal neutral fraction through Ly α radiative transfer, and also bolster arguments for an increasing escape fraction with redshift. With the era of multi-object, near-infrared spectrographs just now beginning, prospects for further solidification of these trends will be strong.

We thank Chuck Steidel and Ian McLain for their hard work in developing the MOSFIRE instrument. The Keck observatory staff proved invaluable, and we thank them for their dedication to maintaining a world-class observatory. We also wish to recognize and acknowledge the very signicant cultural role and reverence that the summit of Mauna Kea has always had within the indigenous Hawaiian community. We are most fortunate to have the opportunity to conduct observations from this mountain.

REFERENCES

Anders, P., & Fritze-v. Alvensleben, U. 2003, A&A, 401, 1063
Bertin, E., Mellier, Y., Radovich, M., Missonnier, G., Didelon, P., & Morin, B. 2002, Astronomical Data Analysis Software and Systems XI, 281, 228
Calzetti, D., Armus, L., Bohlin, R. C., Kinney, A. L., Koornneef, J., & Storchi-Bergmann, T. 2000, ApJ, 533, 682
Davé, R., Oppenheimer, B. D., & Finlator, K. 2011, MNRAS, 415, 11
Davé, R., Finlator, K. & Oppenheimer, B. D. 2012, MNRAS, 421, 98
de Barros, S., Schaerer, D., & Stark, D. P. 2012, arXiv:1207.3663
Faber, S. M., et al. 2003, Proc. SPIE, 4841, 1657
Finkelstein, S. L., et al. 2011, ApJ, 729, 140
Giavalisco, M., et al. 2004, ApJ, 600, L93

González, V., Labbé, I., Bouwens, R. J., Illingworth, G., Franx, M., Kriek, M., & Brammer, G. B. 2010, ApJ, 713, 115
González, V., Labbé, I., Bouwens, R. J., Illingworth, G., Franx, M., & Kriek, M. 2011, ApJ, 735, L34
González, V., Bouwens, R., Ilingworth, G., Labbe, I., Oesch, P., Franx, M., & Magee, D. 2012, arXiv:1208.4362
Grogin, N. A., et al. 2011, ApJS, 197, 35
Hashimoto, T., Ouchi, M., Shimasaku, K., Ono, Y., Nakajima, K., Rauch, M., Lee, J., & Okamura, S. 2013, ApJ, 765, 70
Jones, T., Stark, D. P., & Ellis, R. S. 2012, ApJ, 751, 51
Kelson, D. D. 2003, PASP, 115, 688
Kennicutt, R. C., Jr. 1998, ARA&A, 36, 189
Kuhlen, M., & Faucher-Giguère, C.-A. 2012, MNRAS, 423, 862
Koekemoer, A. M., et al. 2011, ApJS, 197, 36
Labbé, I., et al. 2010, ApJ, 716, L103

TABLE 1
Properties of observed targets

ID	RA	Dec	m_{z850}	z_{spec}	Mass / $[10^9 M_{\odot}]$	SFR $[M_{\odot} \text{ yr}^{-1}]$	E(B-V)	$\log_{10}(\text{age / yr})$	${ m m}_{Ks}{}^{ m b}$
N33_24311	12:37:06.55	62:15:35.4	25.3	3.474	0.8	29.7	0.10	7.48	24.1 ± 0.2
N33_19880	12:36:55.14	62:15:29.2	26.7	3.405	2.3	2.1	0.00	9.16	25.1 ± 0.4
N33_25713	12:37:10.62	62:14:52.6	25.6	3.615	5.7	37.1	0.20	8.26	24.5 ± 0.2
N33_18549	12:36:51.89	62:15:14.5	26.0	3.333	7.7	13.5	0.15	8.86	24.3 ± 0.2
N33_19374	12:36:53.88	62:14:18.0	26.3	3.653	75.7	68.2	0.35	9.16	23.9 ± 0.1
N33_24278	12:37:06.46	62:13:20.5	25.8	3.671	3.7	12.3	0.10	8.56	25.2 ± 0.5
N33_25726	12:37:10.66	62:12:39.0	25.2	3.733	11.5	38.6	0.15	8.56	24.0 ± 0.1
N32_20647	12:36:57.00	62:11:51.0	26.3	3.740	1.1	9.2	0.10	8.16	25.6 ± 0.9
N32_23933	12:37:05.52	62:11:27.2	25.3	3.469	6.8	696.1^{a}	0.45	7.00	23.4 ± 0.1
N32 _ 15359	12:36:43.54	62:11:21.4	24.4	3.488	11.1	1139.7^{a}	0.40	7.00	23.0 ± 0.1
N42_7697	12:36:22.17	62:09:42.3	25.8	3.771	1.2	18.3	0.10	7.86	25.5 ± 0.7
N42_12130	12:36:35.15	62:08:50.8	26.0	3.474	1.7	79.6	0.30	7.36	25.5 ± 0.7
N42_11065	12:36:32.24	62:09:46.5	25.4	3.658	1.4	39.5	0.15	7.59	25.1 ± 0.4
N32_14225	12:36:40.58	62:10:41.1	26.0	3.245	5.8	89.9	0.35	7.86	24.1 ± 0.2
N32 _ 16805	12:36:47.57	62:10:23.7	25.9	3.235	7.2	65.1	0.30	8.11	23.9 ± 0.1
N32_15430	12:36:43.79	62:11:20.0	25.8	3.237	5.1	124.8	0.35	7.65	23.9 ± 0.1
N32_19795	12:36:54.94	62:11:43.8	25.1	2.976	16.1	162.0	0.35	8.06	23.2 ± 0.1
N33_23907	12:37:05.48	62:12:37.1	25.8	3.678	2.0	11.8	0.10	8.31	25.1 ± 0.4
N33_20428	12:36:56.48	62:13:39.9	26.8	3.436	3.4	7.5	0.15	8.76	24.6 ± 0.3
N33_18453	12:36:51.69	62:15:10.1	25.8	3.364	0.2	25.5	0.10	7.00	24.4 ± 0.2

Note. — Sample IDs, coordinates, redshifts, and properties derived from SED fitting. Where appropriate, emission line flux has been subtracted from the K_S -band photometry before fitting to the photometry, using only the stellar continuum to determine SED properties.

 $^{\mathrm{b}}$ Total measured K_S magnitude, including any line emission.

Maiolino, R., et al. 2008, A&A, 488, 463
McLean, I. S., et al. 2012, Proc. SPIE, 8446
McLinden, E. M., et al. 2011, ApJ, 730, 136
Meurer, G. R., Heckman, T. M., & Calzetti, D. 1999, ApJ, 521, 64
Nestor, D. B., Shapley, A. E., Kornei, K. A., Steidel, C. C., & Siana, B. 2013, ApJ, 765, 47
Oke, J. B., & Gunn, J. E. 1983, ApJ, 266, 713
Ono, Y., Ouchi, M., Shimasaku, K., Dunlop, J., Farrah, D., McLure, R., & Okamura, S. 2010, ApJ, 724, 1524
Ono, Y., et al. 2012, ApJ, 744, 83
Pentericci, L., et al. 2011, ApJ, 743, 132
Robertson, B. E., et al. 2013, ApJ, 768, 71
Shapley, A. E., Steidel, C. C., Pettini, M., & Adelberger, K. L. 2003, ApJ, 588, 65
Schaerer, D., & de Barros, S. 2010, A&A, 515, A73
Schaerer, D., & de Barros, S. 2009, A&A, 502, 423
Schenker, M. A., Stark, D. P., Ellis, R. S., Robertson, B. E., Dunlop, J. S., McLure, R. J., Kneib, J.-P., & Richard, J. 2012, ApJ, 744, 179

Shim, H., Chary, R.-R., Dickinson, M., Lin, L., Spinrad, H., Stern, D., & Yan, C.-H. 2011, ApJ, 738, 69
Stark, D. P., Ellis, R. S., Bunker, A., Bundy, K., Targett, T., Benson, A., & Lacy, M. 2009, ApJ, 697, 1493
Stark, D. P., Ellis, R. S., Chiu, K., Ouchi, M., & Bunker, A. 2010, MNRAS, 408, 1628
Stark, D. P., Ellis, R. S., & Ouchi, M. 2011, ApJ, 728, L2
Stark, D. P., Schenker, M. A., Ellis, R., Robertson, B., McLure, R., & Dunlop, J. 2013, ApJ, 763, 129
Steidel, C. C., Erb, D. K., Shapley, A. E., Pettini, M., Reddy, N., Bogosavljević, M., Rudie, G. C., & Rakic, O. 2010, ApJ, 717, 289
Wang, W.-H., Cowie, L. L., Barger, A. J., Keenan, R. C., & Ting, H.-C. 2010, ApJS, 187, 251

^a When SFRs for these objects are estimated using the dust correction from Meurer, Heckman, & Calzetti (1999) and the UV continuum to SFR conversion of Kennicutt (1998), we find much more modest rates of 30 and 150 M_{\odot} yr⁻¹, respectively.

TABLE 2	
MOSFIRE spectroscopic	measurements

ID	$flux_{H\beta}$ [10 ⁻¹⁸ erg/cm/s]	$flux_{[OIII]} [10^{-18} erg/cm/s]$	$EW_{H\beta}$ [Å, rest]	$\mathrm{EW}_{[OIII]}$ [Å, rest]	$v_{neb} - v_{Ly\alpha} [\mathrm{km/s}]^{\mathrm{a}}$	$\frac{flux_{pred,SED}}{flux_{obs}}$
N33_24311	13.5 ± 2.0	99.5 ± 3.2	140^{+240}_{-100}	$1100_{-200}^{+600} \\ 600_{-200}^{+550}$	152	0.91
N33_19880	5.9 ± 1.7	35.9 ± 3.9	89^{+196}_{-35}		4	
N33_25713	7.2 ± 2.3	21.7 ± 4.2	47^{+78}_{-29}	150^{+70}_{-30}	106	
N33_18549	22.5 ± 2.9	38.9 ± 2.5	170^{+240}_{-120}	300^{+100}_{-50}	319	0.74
N33_19374	-3.0 ± 2.7	1.1 ± 4.7	0^{+7}_{-0}	0^{+21}_{-0}	XXX	
N33 _ 24278	-8.6 ± 3.2	32.8 ± 6.4	0^{+20}_{-0}	370^{+190}_{-120}	207	
N33_25726	9.5 ± 3.8	79.9 ± 8.0	$ \begin{array}{c} -0 \\ 40^{+61} \\ -21 \\ 130^{+310} \\ -40 \end{array} $	360^{+60}_{-50}	86	
N32_20647	9.8 ± 3.6	56.2 ± 7.3	130^{+310}_{-40}	890^{+690}_{-320}	113	
N32_23933	14.0 ± 2.5	49.1 ± 3.8	40^{+49}_{-30}	150^{+20}_{-20}	195	2.31
N32_15359	11.9 ± 2.1	54.8 ± 5.0	21^{+26}_{-17}	100^{+10}_{-10}		1.39
$N42_7697$	7.9 ± 6.2	18.6 ± 9.2	91^{+226}_{-5} 65^{+196}_{-7}	260^{+220}_{-160}	227	
N42_12130	5.5 ± 3.3	6.0 ± 4.4	65^{+196}_{-7}	150^{+210}_{-90}	XXX	
N42_11065	2.0 ± 4.3	1.2 ± 7.3	4^{+80}_{-1}	150_{-90}^{+210} 6_{-3}^{+113}	XXX	18.74
$N32_14225$	7.2 ± 3.5	47.6 ± 9.0	32^{+65}_{-18}	280^{+100}_{-80}		
N32_16805	20.7 ± 12.0	39.6 ± 5.8	79^{+162}_{-29}	190^{+50}_{-40}		1.42
$N32_15430$	11.3 ± 3.7	68.6 ± 5.2	50^{+82}	340_{-50}^{-40}		1.01
$N32_19795$	8.4 ± 6.9	94.2 ± 7.5	17_{-4}^{+29}	190^{+20}_{-20}		1.60
N33_23907	6.0 ± 4.9	18.3 ± 6.3	54_{-3}^{+139}	210_{-120}^{+200}	XXX	
N33_20428	8.1 ± 3.2	45.6 ± 4.9	84^{+164}_{-32}	500^{+280}_{-120}		
N33_18453	9.6 ± 1.7	126.5 ± 3.9	320^{+860}_{-150}	4400_{-2000}^{+6200}		1.63

Note. — MOSFIRE emission line measurements for our sample.

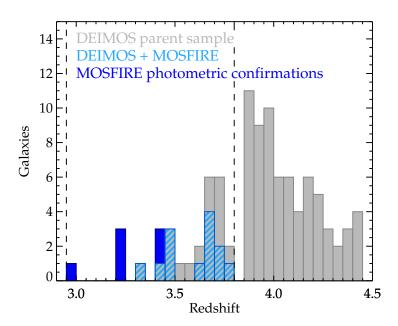


Fig. 1.— Redshift distribution of Lyman Break Galaxies targeted with MOSFIRE. The grey histogram indicates the parent sample within GOODS-N from our prior DEIMOS campaign. The light blue cross-hatched histogram denotes the subset of the DEIMOS spectroscopic sample studied with MOSFIRE and the dark blue histogram that drawn from a photometric selection (see Section 2). Dashed lines show the boundaries within which $[O\ III]$ is expected to contaminate the K_S photometry.

^a 'xxx' denotes DEIMOS objects for which the MOSFIRE emission lines were not robust enough to permit a velocity offset measurement. '...' denotes objects from our photometric sample.

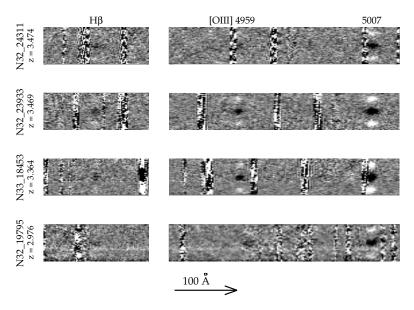


Fig. 2.— Example 2-D MOSFIRE spectra in A-B-A format for 4 targets showing prominent nebular emission. The left panels focus on the region containing H β and the right panels the [O III] doublet (marked).

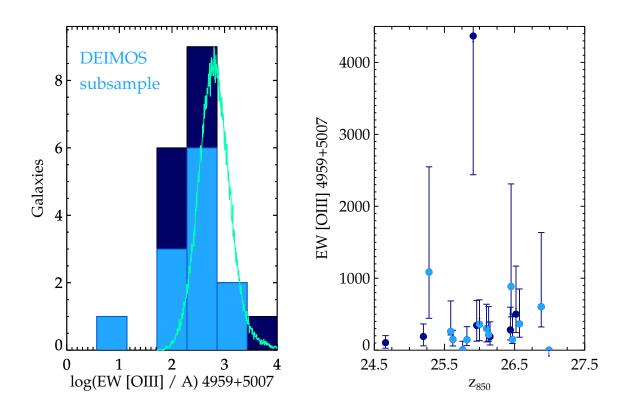


Fig. 3.— Left: The rest-frame equivalent width distribution of [OIII] 4959 + 5007 Å derived from our MOSFIRE spectroscopic data. The green curve estimates the distribution expected from the distribution for H α derived from SED fitting method by Stark et al. (2013). Right: Individual equivalent widths of [O III] versus z_{850} magnitude. In both panels, light blue denotes the spectroscopic sample and dark blue the photometric sample (see Section 2).

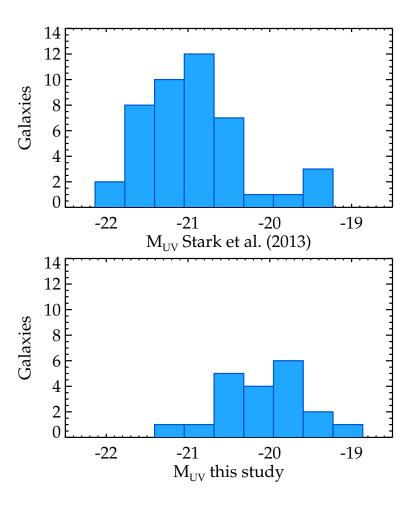


Fig. 4.— Absolute UV magnitude distribution for the 3.8 < z < 5.0 sample discussed by Stark et al. (2013) (top panel) compared to that at 3.0 < z < 3.8 studied in this paper.

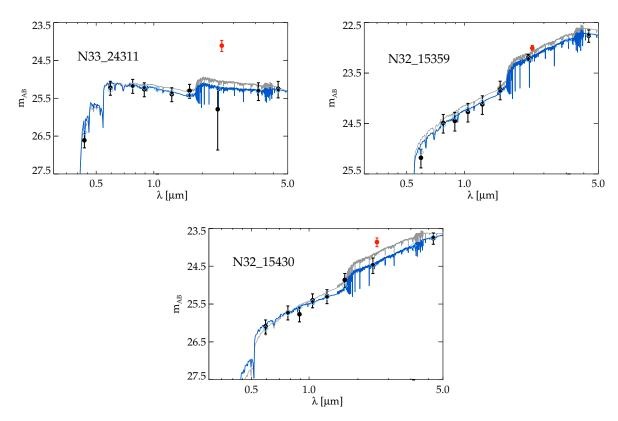


Fig. 5.— Spectral energy distributions for three of our targets. The red data point represents the observed K-band photometry without correction for [O III] contamination, and the grey spectrum shows the best fit SED to this data. The black K-band data point shows stellar continuum flux after correction for the MOSFIRE-determined [O III] line flux, and the blue spectrum is the associated best fit SED.

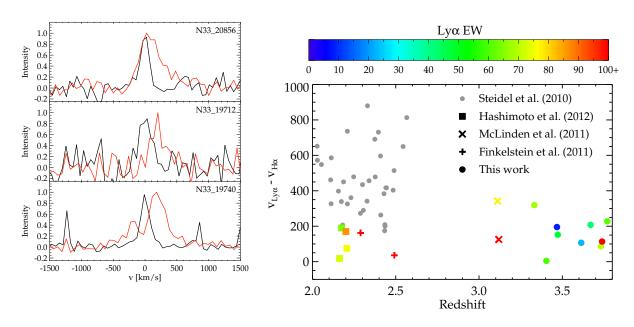


Fig. 6.— Left: The velocity structure observed by comparing MOSFIRE and DEIMOS spectra for three objects from our spectroscopic sample. Zero velocity is defined using a stack of the nebular [OIII] and H_{β} lines, shown in black. Ly α is overlaid in red, arbitrarily scaled in the y-axis. Right: Compilation of Ly α velocity offset measurements from various sources in the literature. Our objects show much more modest offsets than the sample of Steidel et al. (2010), which all display only low level Ly α emission, but are more consistent with numerous LAEs from the literature, also plotted.